Energy Storage Materials xxx (xxxx) xxx

Contents lists available at ScienceDirect

Energy Storage Materials

journal homepage: www.elsevier.com/locate/ensm

Surface enriched graphene hollow spheres towards building ultra-high power sodium-ion capacitor with long durability

Ranjith Thangavel [a,b], Aravindaraj G. Kannan [c], Rubha Ponraj [c], Gabin Yoon [d], Vanchiappan Aravindan [e], Dong-Won Kim [c], Kisuk Kang [d], Won-Sub Yoon [a], Yun-Sung Lee [b,*]

[a] Department of Energy Science, Sungkyunkwan University, Suwon, 440-746, South Korea
[b] School of Chemical Engineering, Chonnam National University, Gwang-ju, 61186, Republic of Korea
[c] Department of Chemical Engineering, Hanyang University, Seoul, 04763, Republic of Korea
[d] Department of Materials Science and Engineering, Seoul National University, Seoul, 151-742, Republic of Korea
[e] Department of Chemistry, Indian Institute of Science Education and Research (IISER), Tirupati, 517507, India

ARTICLE INFO

Keywords:
Na-ion capacitor
Carbon anode
Sodium ion battery
DFT calculation
Heteroatom

ABSTRACT

We report the synthesis and fabrication of all carbonaceous electrode based high-energy and high-power- sodium-ion capacitors (NICs) which are anticipated to bridge the gap between rechargeable batteries and double layer capacitors. Unfortunately, the kinetic imbalance between battery type electrode and capacitive cathodes severely restricts the energy–power capabilities of NICs. To circumvent the kinetic mismatch and boost the efficiency of NICs, we are utilizing the rationally designed graphene hollow nanospheres (GHNS) as a bi-functional electrode in which nitrogen and sulfur atoms are infiltrated through the carbonaceous matrix. This eventually results in enhanced Na-ion storage capacity of GHNS which is paralleled by density functional theory calculations owing to the binding ability. All GHNS based NIC displays a high operating voltage, high energy density, and high power density, for example, the energy densities of 121 Wh kg^{-1} at the power density of 100 W kg^{-1}. Further, the NIC can render remarkable cycling stability of ~85% retention after 10,000 cycles (~0.0015% energy decay per cycle) and emphasized to be used as a potential candidate for hybrid charge storage systems in the near future.

1. Introduction

Over the past decades, lithium-ion batteries (LIBs) have efficiently served as promising charge storage technology towards portable electronic devices, and attempts are being made exploit them in zero emission transportation applications [1,2]. Nevertheless, the limited and expensive lithium resources greatly restrict the application of LIBs in next-generation large-scale storage devices such as electric vehicles and smart grids. Recently, sodium-ion batteries (SIBs) have emerged as a potential alternative to LIBs because of the similar working chemistry as well as sodium abundance; substantial success has been achieved with high-performance cathodes and anodes, and SIBs are on the verge of commercialization [3–5]. Of course, few startups already announced the commercialization of their prototypes, for example, Faradion from UK and Tiamat from France.

The inferior Na-ion kinetics of batteries can be efficiently tackled with the use of high-power supercapacitors in many applications. On the other hand, the energy demands for next-generation applications cannot be satisfied with the existing state-of-the-art high-energy batteries, whereas the high-power capacitors failed to translate such energy owing to the physisorption mechanism. This necessitates clearly alert us to develop new charge storage devices with high energy and power capabilities [6]. Also, this bridging the performance gap between the batteries and supercapacitors. Sodium-ion capacitors (NIC) is considered as a promising and emerging device which can effectively overcome the barriers of rechargeable batteries and conversional electric double layer capacitors in terms of low power capability associated with limited cycle life and inferior energy density, respectively [7,8].

As a result, the NIC composed of high energy–high power characteristics because of two different charge-storage mechanisms involved during the charge storage process. The working mechanisms are predominantly based on Na-ion insertion/extraction in the battery-type anode and the simultaneous anion adsorption/desorption on the counter electrode [9,10]. Till date, numerous battery type materials such as metal oxides, polyanions, and hard carbon have been explored for NIC applications [11,12]. On the other hand, various high surface area

* Corresponding author.
E-mail address: leeys@chonnam.ac.kr (Y.-S. Lee).

https://doi.org/10.1016/j.ensm.2019.09.016
Received 17 June 2019; Received in revised form 13 August 2019; Accepted 12 September 2019
Available online xxxx

carbonaceous materials such as activated carbon, biomass-derived carbon, carbon nanotubes (CNTs), and graphene have been reported for the capacitor-type electrode [13,14].

To date, most of the research has been devoted to the exploration of new materials for battery and capacitor type electrodes towards constructing high performance NICs, but very less research work only focused on addressing the kinetic issues. Since the kinetic mismatch between the dissimilar electrodes greatly undermines the performance of NICs, thereby curtailing the realization of high energy at ultra-high powers as well as superior stability [15,16]. The fabrication of NICs with identical electrodes that can simultaneously function as battery-type and capacitor-type electrodes is one of the effective solutions to mitigate the issue. Energy storage devices comprising symmetrical electrodes fabricated with $Na_3V_2(PO_4)_3$, $Na_{0.44}MnO_2$, $Na_3MnTi(PO_4)_3$, and $Na_{0.8}Ni_{0.4}Ti_{0.6}O_2$ have been recently explored, but sluggish, bulk intercalation kinetics hampers the translation of high voltage, high energy, and high power [17–19]. Several state-of-the-art capacitors dissipate a large amount of energy below a power density of 5 kW kg^{-1} and fail to retain the similar characteristics above 20 kW kg^{-1}. Performance at harsh condition is essential for next-generation applications, especially electric vehicles [7,9,10,15]. Exploring nanomaterials-with high capacity and surface charge storage-that can efficiently function in a wide operating window is the key to address performance issues in NICs.

Carbonaceous electrodes are potential candidates for battery and capacitor electrodes owing to the high electrical conductivity, chemical stability, facile charge storage mechanism, tunable porosity, nontoxicity, and sustainability [20–22]. A variety of carbonaceous materials including expanded graphite, hard carbon, carbon spheres, porous carbon, nitrogen-doped carbon, carbon nanosheets, carbon fibers, and carbon quantum dots have been investigated as anodes for SIBs [23–25]. Despite this progress, there is a wide room for the development of nanostructured carbon materials with improved performance, which can be achieved by studying the influence of heteroatoms on storage kinetics.

The prominent mechanism of Na-ion storage in carbonaceous materials is based on the combination of both Faradaic and non-Faradaic process; however, insertion of Na-ions into expanded graphitic structures is generally diffusion-limited, and adsorption occurs on the surface defects/functional groups and voids [26]. Therefore, the utilization of surface-mediated storage is important to realize stable performance electrode towards NIC perspective with high energy and power. This requires not only in materials but also with the engineering aspect to achieve effective utilization of carbonaceous electrodes towards surface moieties and facile ionic transport. Parallelly, two-dimensional materials gained a special interest in fast Na-ion storage including graphene [27]. Designing the material with hollow architecture, and in turn, enhanced surface utilization, as well as shorter diffusion pathways, is one of the effective ways to overcome the present performance challenges. In addition, high porosity and the presence of active surface sites on the carbonaceous material can lead to the realization of excellent capacitive behavior to employ as a capacitor type electrode. Few research groups have attempted to construct the template mediated porous graphene framework for energy storage applications (battery and capacitor applications separately) but failed to achieve a highly interconnected graphene nano sphere architecture and the desired performance [20,25,28,29]. Therefore, designing a perfect 3D interconnected hollow nanostructures can be used as an effective bi-functional electrode, and are attracting immense attention for application in energy storage devices.

We herein demonstrate the electrochemical activity of highly-interconnected hollow graphene nanospheres with dual heteroatoms (nitrogen and sulfur) as both anode and cathode for the fabrication of NICs. The self-assembly of nitrogen and sulfur doped 2D graphene into a highly connected 3D hollow architecture using a facile sacrificial template method enables facile Na-ion storage kinetics and imparts high active site exposure to the electrolyte. N and S-atoms were utilized owing to the high electronegativity and larger atomic size, respectively, which results in the alteration of the structure, charge and spin densities of carbon, favoring enhanced activity. Moreover, the incorporation of functional heteroatoms into the graphene framework enhances the electrolyte wettability of the electrode surface, and creates more active defect sites. By merging the advantages of hollow 3D architecture with high porosity, high surface area, and a high degree of dual-heteroatom doping, we have achieved a new high-performing NIC. Interestingly, such dual-heteroatom doped 3D carbon nanostructures have not been investigated for Na-ion capacitor applications. The all nanocarbon NIC exhibits the maximum energy density of 121 Wh kg^{-1} and displays outstanding stability of 10,000 cycles (~85% retention). Thus, the realization of NS-GHNS//NS-GHNS full-cell NICs indicates that all carbon nano-architectures based configuration are highly promising for the development of a next-generation hybrid charge storage device and discussed in detail.

2. Results and discussion

Fig. 1 illustrates the schematic representation of the synthesis procedure for the preparation of NS-GHNS. Accordingly, first, GO wraps around the amino-functionalized silica sphere templates via electrostatic interactions between the positively charged amino groups on the silica template and the negatively charged oxygen functional groups on GO. A positive – negative charge interaction is always essential and crucial for wrapping up the template with the precursor. It is very complicated to develop a hollow architecture without such interactions. The presence of thiourea effectively reduces the GO in to reduced graphene oxide (rGO) which not only serves as a reducing agent, and also serves as a source for both nitrogen and sulfur atoms.

The SEM and TEM image of SiO_2 template used for GHNS synthesis are shown in Fig. 1a and b respectively. The SiO_2 template shows a uniform spherical morphology and the pore size distribution in Fig. S1a shows that the average size of the SiO_2 template is mainly distributed between 210 – 240 nm. The uniform coverage of silica templates by rGO nanosheets is evident from the TEM images (Fig. 2c -d). The strong electrostatic interaction between GO nanosheets and amino-functionalized silica templates enables the uniform coverage of templates by rGO nanosheets. Finally, the NS-GHNS sample is obtained by etching the silica template using hydrofluoric acid. The SEM images (Figs. S1c and S1d), and TEM images in Fig. 1e–f clearly depict the hollow spherical morphology of rGO sheets after template removal. Furthermore, the images clearly reveal that the hollow nanospheres are highly interconnected which is critical for the continuous and facile electron transport. Notably, the highly interconnected architecture is attributed to the two-dimensional (2D) nature of GO; dimensionally large GO sheets wrap around the silica templates and connect them. In addition, the hollow morphology is maintained even after the template removal, which can be attributed to the mechanical robustness of rGO nanosheets. TEM-EDS elemental mapping (Fig. 2g) clearly depicts the uniform distribution of carbon, oxygen, nitrogen, and sulfur. The HR-TEM images on Fig. S2 reveals the few layered nature of GHNS, and NS-GHNS that can favors fast pseudocapacitive Na-ion storage [24,30]. It is worth mention that the GO-SiO_2 template mass ratio is crucial to attaining a highly interconnected spherical architecture. However, at low ratios (*i.e.,* excess of silica template), the highly interconnected nature of GHNS is not well retained whereas, at high ratios (*i.e.,* excess of GO), wastage of GO is noted during the centrifugation step (Fig. S3).

The NS-GHNS sample exhibits a Type IV N_2 adsorption/desorption isotherm with a hysteresis loop (Fig. 3a), confirms the co-existence of micro and mesopores. The BET surface area of NS-GHNS is calculated to be ~320 $m^2 g^{-1}$ with a pore volume of 1.32 $cm^3 g^{-1}$, indicating the highly porous nature of the resultant material. Presence of porous nature certainly offers a large number of electrolyte reservoir sites and provides channels for fast Na-ion transport [31,32]. The Raman spectra of GO and NS-GHNS in Fig. 3b show the characteristic D and G bands attributed to sp^3 distortions in disordered carbon and sp^2 hybridized graphitic carbon, respectively. The D band is centered around ~1358 cm^{-1} for both GO

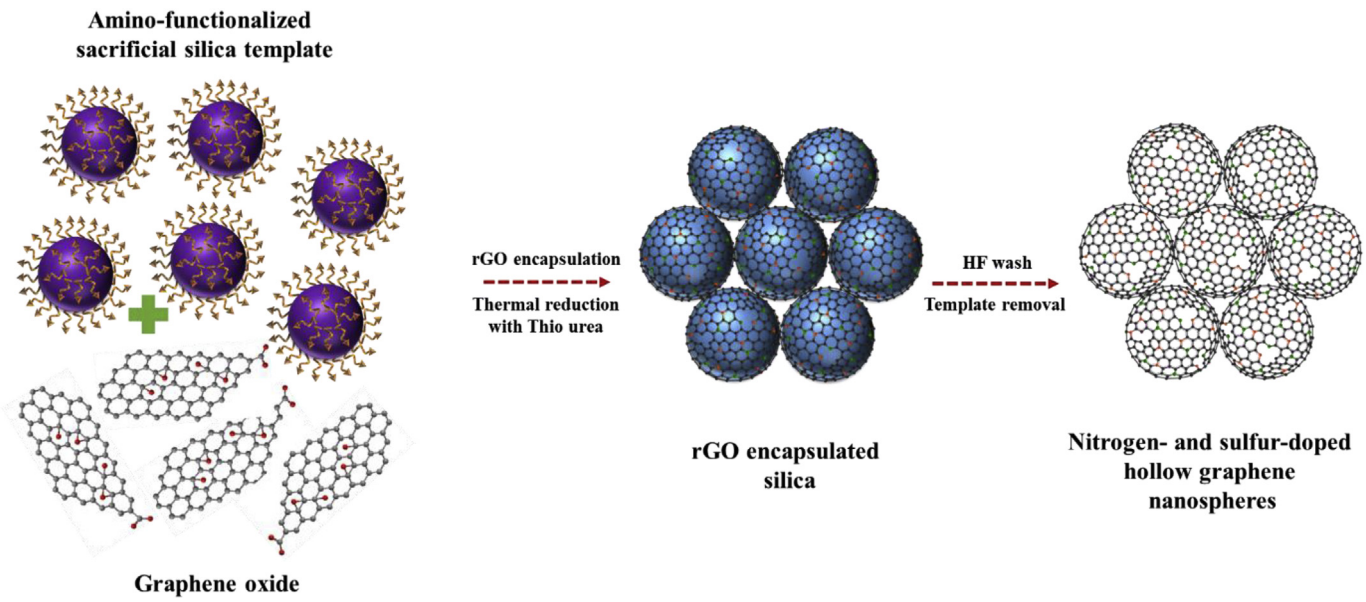

Fig. 1. Schematic illustration of the synthesis of NS-GHNS by a sacrificial template method.

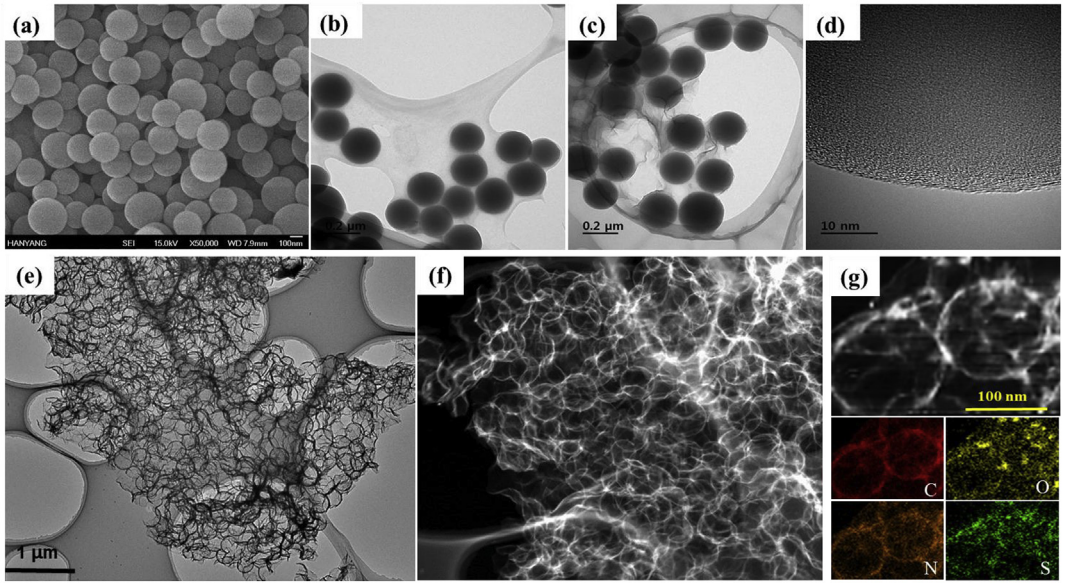

Fig. 2. (a) SEM image of SiO_2 template, and TEM images (b) SiO_2 template, (c)–(d) rGO encapsulated SiO_2, (e)–(f) NS-GHNS, (g) EDS elemental maps of NS-GHNS.

and NS-GHNS; however, the G band shows a red shift from ~1600 cm^{-1} (GO) to ~1590 cm^{-1} (NS-GHNS), which is attributed to *n*-type substitutional doping of graphene with N- and S- heteroatoms. The I_D/I_G ratio is also calculated to be ~0.96 and ~1.12 for GO and NS-GHNS, respectively. The increase in I_D/I_G after GO reduction is attributed to a reduction in the average size of sp^2 domains and the increase in defective sites after heteroatom incorporation [33,34].

We have studied the surface chemical composition of NS-GHNS using XPS (Fig. 3c). The XPS survey spectrum of NS-GHNS exhibits N 1s and S 2p peaks, indicating the successful incorporation of N- and S heteroatoms into the graphene framework. The chemical composition of NS-GHNS is determined to be 85.39 at.%, 9.45 at.%, 1.82 at.%, and 3.34 at.% of carbon, oxygen, sulfur, and nitrogen, respectively. The heteroatom doping eventually improves the electrical conductivity which is anticipated to suppress the huge irreversible capacity loss during the initial cycles. Nevertheless, a large number of heteroatom functional groups on graphene possibly favor fast surface-mediated Na-ion storage [30,35]. The deconvoluted C 1s spectrum (Fig. 3d) shows a peak at ~284.6 eV, confirming the presence of sp^2 hybridized carbon [36,37]. The peak located at ~ 285.8 eV confirms the presence of C–O, C–N, and C–S. In addition, the peak positioned at ~288.9 eV is attributed to C=O, indicating the presence of carboxyl and carbonyl groups in NS-GHNS. The deconvoluted N 1s spectrum (Fig. 3e) shows three peaks at ~398.5, 399.9, and 401.2 eV, which corresponds to pyridinic, pyrrolic, and graphitic nitrogen, respectively. The graphitic nitrogen is well known to improve the electronic conductivity of NS-GHNS by contributing more electrons to the π-conjugated carbon structure while pyridinic and pyrrolic nitrogen can create some defects on NS-GHNS structure and greatly improve the capacitive storage of the carbon structure by inducing electron-donor effect. The S 2p spectrum is resolved into three peaks at ~164.3, 165.8, and 167.4 eV, which are attributed to C–S–C $2p_{3/2}$, C–S–C $2p_{1/2}$, and SO_x type sulfur, respectively (Fig. 3f). The sulfur defects on carbon structure can provide active Na^+ storage sites channels. The existence of two heteroatoms is anticipated to synergistically enhance the

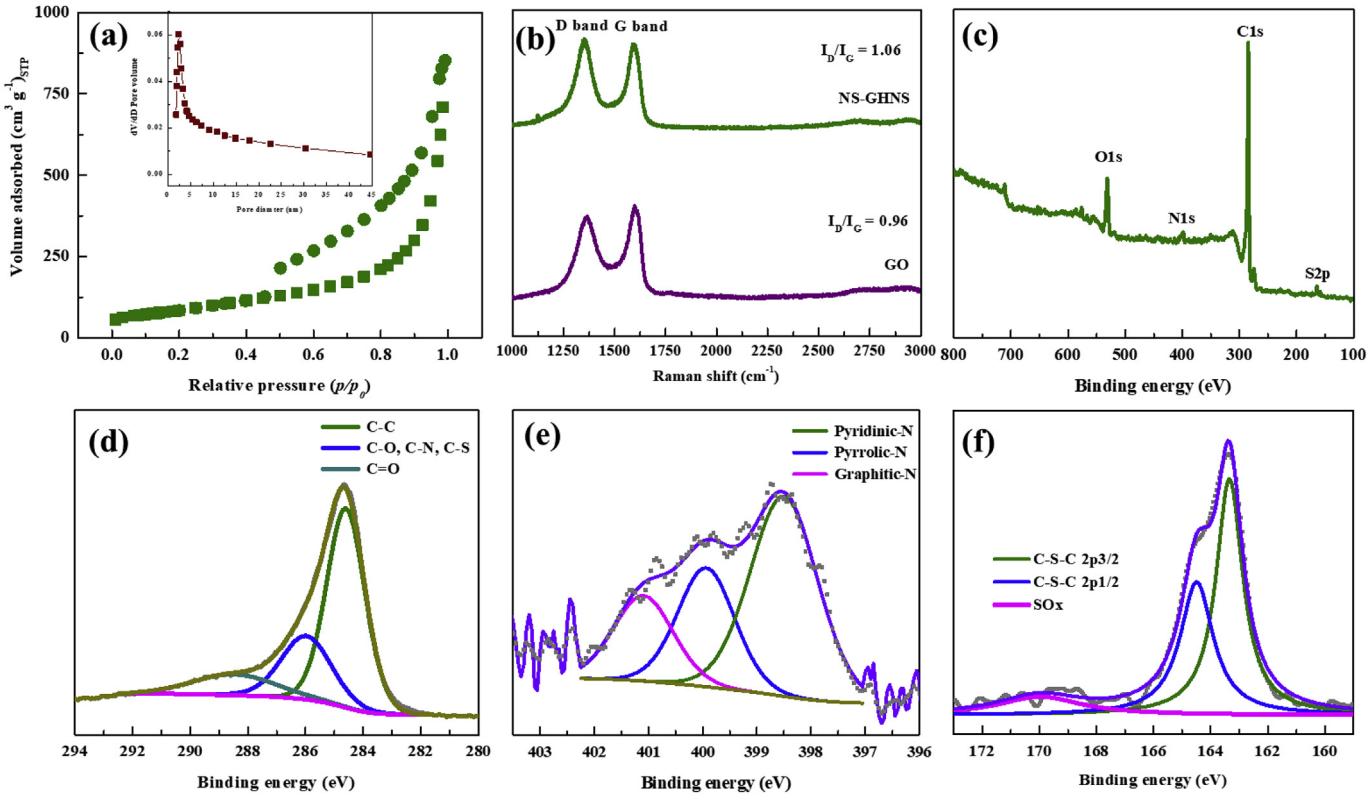

Fig. 3. Physical characterization: (a) N_2 adsorption/desorption isotherms of NS-GHNS, (b) Raman spectra of NS-GHNS and GO, (c) XPS survey spectra of NS-GHNS, and high-resolution deconvoluted XPS spectra of (d) C1s, (e) N1s, and (f) S2p.

surface wettability and electrical conductivity which eventually serves as active sites for facile Na-ion storage [35].

2.1. Anodic performance

Fig. 4a shows the galvanostatic charge/discharge (CD) profiles of NS-GHNS at 0.5 A g^{-1} in the potential range 0.01–3 V *vs.* Na/Na$^+$. The first discharge and charge capacities of NS-GHNS are 760 mAh g^{-1} and 272 mAh g^{-1}, respectively with a corresponding coulombic efficiency of ~36%. The initial irreversible capacity loss is mainly due to the formation of a solid electrolyte interface (SEI) layer and an irreversible reaction between the carbon functional groups and sodium ions, which is very common for carbonaceous anodes. However, this can be minimized by altering the electrolyte solution with tailored composition, and by metal oxide deposition over carbon surface [38,39]. Recently, ether based electrolytes have gained much attention for Na$^+$ storage in carbon based anodes due to the formation of stable, and uniform interface. However, the compatibility of ether based electrolytes with several inorganic cathodes must be addressed to realize porotype full-cell [40,41]. The poor oxidative stability of ether based electrolytes also needs to be addressed when working with high voltage sodium-ion storage devices [9]. Nevertheless, the discharge capacity stabilizes within a few cycles, and the coulombic efficiency approaches >99%. After 1000 cycles, the NS-GHNS sample maintains a high discharge capacity of ~264 mAh g^{-1}, depicting stable Na-ion storage capability (Fig. 4b). The CD curves show a sloping voltage profile, *i.e.,* non-linear behaviour, indicating that the capacity contribution is mainly due to sodium storage into graphene layers [42]. The Na ion storage mechanism mainly involves adsorption/desorption at planar surfaces, pseudo-capacitive storage on the graphene edge/defect sites, and Na$^+$ intercalation into graphene interlayer. Also, the surface contribution and influence of crystallinity for the sustained Na-storage cannot be ruled out. This is in contrast to the voltage profile exhibited by hard carbon materials, wherein a low-potential plateau appears close to the reference electrode potential (Na/Na$^+$). The absence of such low-potential plateau for NS-GHNS indicates that the material overrides the risks due to sodium plating/stripping, thereby making the NS-GHNS anode suitable for long-term usage [43]. On the other hand, the pristine GHNS delivered a first CD capacity of (Fig. S4) 240 mAh g^{-1} and 849 mAh g^{-1}, respectively and corresponding coulombic efficiency of ~28.2%. The higher coulombic efficiency of NS-GHNS is attributed to the decreased oxygen functionalities on the surface due to nitrogen and sulfur doping [44]. As mentioned, the dual heteroatoms eventually improve electronic conductivity and thereby enhancing the Na-ion storage capability by providing additional active sites. Fig. 4c compares the rate performances of NS-GHNS and pristine GHNS. Apparently, the NS-GHNS anode delivers a higher discharge capacity than the pristine GHNS anode at all current densities. Furthermore, excellent capacity retention is clearly evident when the electrode is switched again at lower current densities from higher rates. Fig. 4d compares the performance of NS-GHNS with those of previously reported carbon anodes and clearly depicts the superiority of NS-GHNS [45,46]. The capacity exhibited by NS-GHNS is far superior to that of several previously reported carbonaceous anodes such as hard carbon, hollow carbon spheres, hollow carbon wires, carbon nanosheets, carbon nanofoams, carbon/graphene composite, and 3D porous carbon.

Further, we have studied the influence of reduction temperature by comparing the above results (for the sample synthesized at 700 °C: NS-GHNS-700) with those of samples synthesized at 600 °C (NS-GHNS-600) and 800 °C (NS-GHNS-800) (see Fig. 4e). NS-GHNS-600 shows a higher capacity than NS-GHNS-700 at lower current rates (0.1–1 A g^{-1}), whereas the NS-GHNS-700 exhibits a rapid capacity decay at low current rates. For instance, NS-GHNS-600 shows a high discharge capacity of ~630 mAh g^{-1} at 0.1 A g^{-1} but a low discharge capacity of ~32 mAh g^{-1} at 20 A g^{-1}. NS-GHNS-800 shows a discharge capacity similar to that of NS-GHNS-700 at low current rates whereas at higher rates (20 A g^{-1}) the discharge capacity of ~75 mAh g^{-1} only observed which is lower

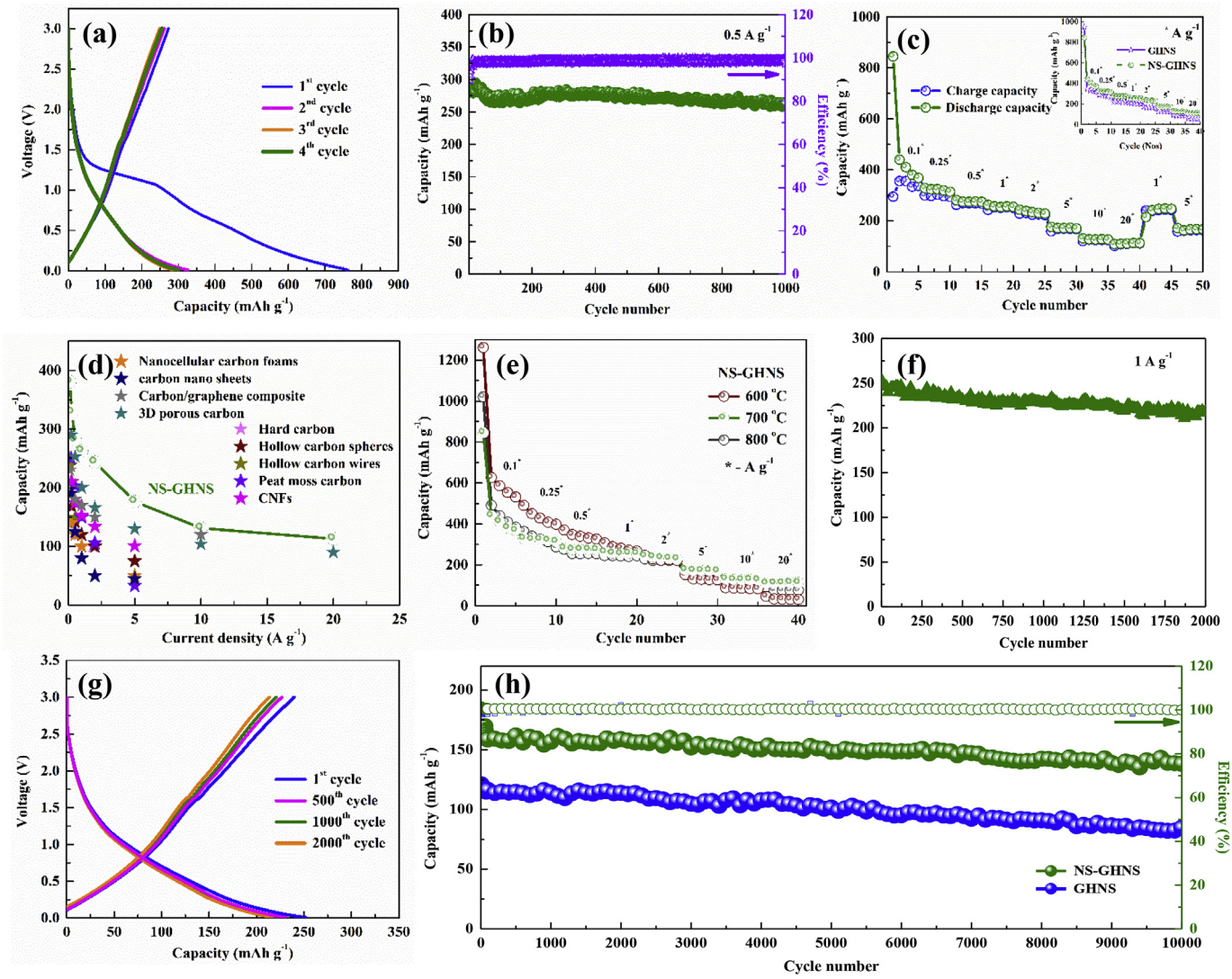

Fig. 4. Anodic performance of NS-GHNS: (a) Charge/discharge profiles at 0.5 A g^{-1}, (b) Cycling stability at 0.5 A g^{-1}, (c) Rate performance, (d) Performance comparison with other carbon anodes, (e) Rate performance of NS-GHNS synthesized at different temperatures, (f) Cycling stability at 1 A g^{-1}, (g) Charge/discharge profiles at different cycles (1 A g^{-1}), and (h) Cycling stability at 5 A g^{-1}.

than that of NS-GHNS-700 at higher rates (~112 mAh g^{-1}).

By considering the overall view, the NS-GHNS prepared at 700 °C rendered excellent performance, which exhibits high capacity and high current stability. This is mainly because of the higher electrical conductivity of graphene sheets, and a large number of active Na-ion storage sites provided by the hollow structured architecture [23]. Further, the highly interconnected hollow architecture ensures the continuous flow of electrons and greatly shortens the Na-ion diffusion distance. Hence, high capacity is realized even without the inclusion of conductive carbon network which enormously enhances the charge transfer reaction rate, and leads to ultra-fast rate performance [47]. Furthermore, the doped heteroatoms in the graphene framework favor electrolyte ion adsorption and rapid ion transfer kinetics, contributing to the outstanding rate performance along with synergistically enhance the electrical conductivity and surface wettability of NS-GHNS. As a result, interfacial resistance will be diluted for NS-GHNS which is clearly paralleled by Nyquist plots (Fig. S5). Furthermore, Nyquist impedance spectra of NS-GHNS samples synthesized at different temperature is also analyzed (Fig. S6). NS-GHNS (700 °C) showed a low charge transfer resistance and low electrode-electrolyte resistance than NS-GHNS (600 °C) and NS-GHNS (800 °C), indicating improved electron-transfer kinetics in NS-GHNS (700 °C).

The high capacity and rapid capacity decay at lower current rates for NS-GHNS-600 are attributed to the numerous oxygen functionalities (see the XPS data, Fig. S7). Although the oxygen functionalities provide a large number of Na-ion storage sites, but it causes severe electrolyte decomposition and results in high irreversibility. The high capacity decay and low initial coulombic efficiency is a common phenomenon observed in low conductive and disordered carbon materials, which are usually synthesized at low temperatures [23,24]. For instance, the electronic conductivity of NS-GHNS-600 is generally low because of the presence of a large number of oxygen functionalities; therefore, it displays poor performance at high current rates [23,24]. On the other hand, the poor performance of NS-GHNS-800 at high current rates is attributed to the enhanced graphitization of the material at high temperatures. The HR-TEM images of NS-GHNS-600 and NS-GHNS-800 is given in Fig. S8. A decrease in heteroatom content in NS-GHNS-800 adversely affects the Na-ion storage kinetics [44,48]. Thus, NS-GHNS synthesized at 700 °C is an optimum condition to yield a high performance material towards building high-energy, and high-power NIC with good cycling profile.

To obtain a deeper insight into the rapid Na-ion storage kinetics of NS-GHNS (700 °C), CV analysis was carried out at different scan rates. The CV in is broad (Fig. S9a); they display a long cathodic slope between 1.5 V and 0.01 V and a broad anodic counterpart peak. During sodium

storage, the broad anodic and cathodic peak intensity increases with scan rate (v), which is in accordance with the power law $i = av^b$, where i is the current (A), and a and b are adjustable parameters. A b value close to 0.5 indicates a diffusion-limited reaction; when b approaches 1, the reaction becomes surface-limited [49]. From the CV curves, the b values are determined to be 0.89 and 0.83 for anodic and cathodic peaks, respectively, indicating that the major capacity contribution during sodium storage is surface-limited. Furthermore, the quantitative storage contribution for NS-GHNS can be evaluated from the relationship $i(V) = k_1\nu$ (capacitive) + $k_2\nu^{1/2}$ (diffusion-limited), where k_1 and k_2 are the appropriate constants acquired from linear plots of $\nu^{1/2}$ *vs.* $i/\nu^{1/2}$ at a certain voltage (Fig. S9b) [49]. For example, at the scan rate of 1 mV s^{-1}, the surface-limited contribution to the total capacity is ~86%, and the diffusion-limited process is ~14%. The large surface-mediated capacity contribution arises from the high surface area hollow architecture of NS-GHNS with mesopores that provide numerous Na-ion storage sites and allow fast diffusion at high current rates [50]. Moreover, the defective sites resulting from N and S heteroatom incorporation enhance the electrode surface-electrolyte interaction and favor the surface-mediated sodium storage, also increases the polarity between the graphene layers, thereby facilitating a facile graphene sheet-electrolyte contact [51].

To further analyze the performance of NS-GHNS (700 °C), we evaluated the durability at two different current densities. Fig. 4f–g show the sodium storage capability of NS-GHNS at 1 A g^{-1}. The voltage profile displays a sloping behavior (similar to that mentioned earlier); it is well maintained throughout the cycles, indicating the stable performance of NS-GHNS. In addition, the sample exhibits a capacity of ~218 mAh g^{-1} with >99% coulombic efficiency even after 2000 cycles (Fig. 4f). At 5 A g^{-1}, the NS-GHNS anode remarkably delivers a discharge capacity of ~141 mAh g^{-1} after 10000 cycles by maintaining the extremely high coulombic efficiency (>99%) with capacity retention of ~86% (Fig. 4h). With regard to durability, the NS-GHNS anode outperforms several previously reported anodes for SIBs; such high durability is very difficult to materialize in alloy-type anodes, especially Sb and its derivatives due to the unusual volume variation and associated pulverization upon cycling [8,9]. In contrast, the pristine GHNS anode delivers inferior capacity retention under the same test conditions. The high capacity retention for the NS-GHNS anode is attributed to an enhancement in the electrolyte-electrode interaction after heteroatom incorporation, resulting in a continuous supply of Na-ions for facile storage. Favorable surface functionalities over carbon surface are very essential to increase the surface wettability of the electrode by an electrolyte. Enhanced wettability is highly favorable for reducing the interface resistance between electrode-electrolyte, ion diffusion losses, and efficient ion storage at high current rates. The nitrogen and sulfur hetero atoms in NS-GHNS could greatly alleviate the surface wettability, allowing the electrolyte to penetrate deeper into micropores, thereby allowing a large number of sites for facile Na^+ storage [51]. To understand the high durability of the NS-GHNS anode, we subjected it to post-mortem analysis after cycling. The TEM images in Fig. S10 reveal that the hollow nanosphere morphology of NS-GHNS remains intact even after repeated cycling, depicting the structural integrity and the non-destructive Na-ion storage mechanism. A table comparing the anodic performance of GHNS, and NS-GHNS is given in Table S1.

We have performed density functional theory (DFT) calculations to understand the origin of the excellent performance of NS-GHNS [52–56]. To evaluate the Na-ion binding energy of 3D hollow carbon

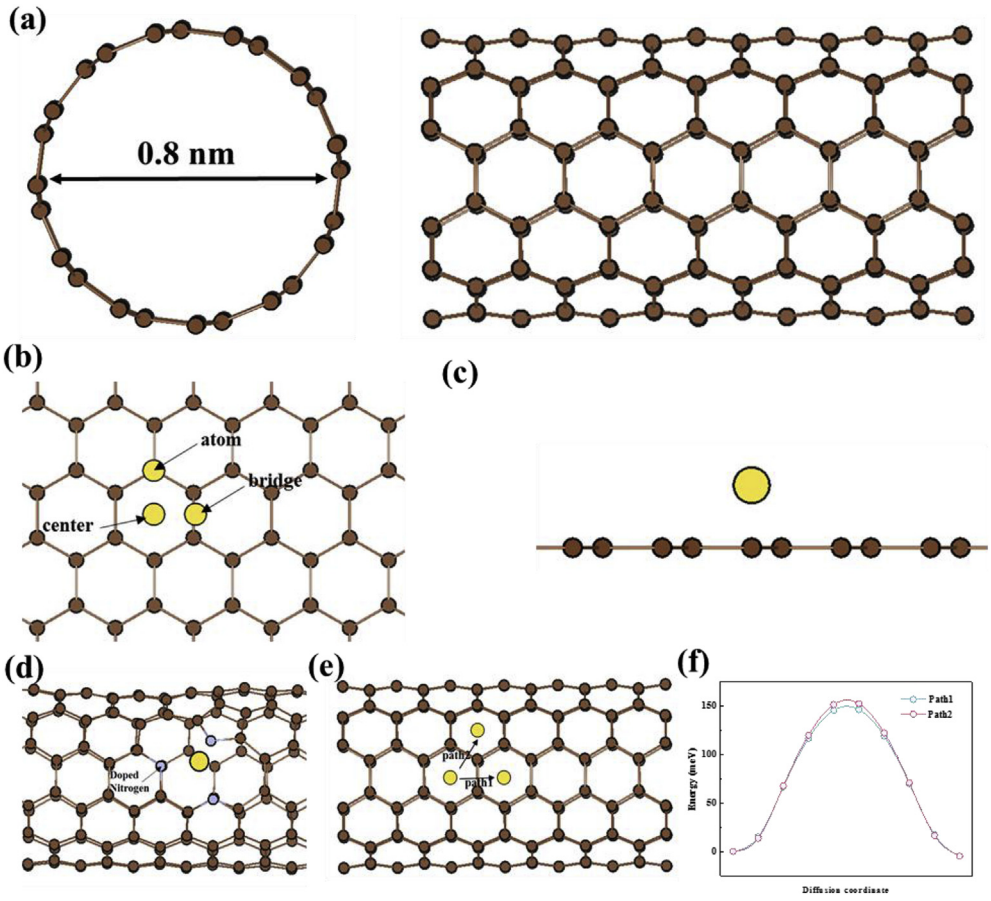

Fig. 5. First-principles studies: (a) Schematic illustration of the GHNS model; (b–d) Graphical illustration of Na-ion binding to different binding sites on (b) GHNS, (c) planar graphene, and (d) NS-GHNS; and (e–f) Illustration of Na-ion diffusion paths at the surface and the corresponding energy profiles. Brown and yellow circles represent C and Na atoms, respectively. (For interpretation of the references to colour in this figure legend, the reader is referred to the Web version of this article.)

nanostructures (GHNS and NS-GHNS), CNT frameworks, which have curved surfaces similar to spheres, are taken as 3D models for the calculations by employing periodic boundary conditions (Fig. 5a). Three different sites at the surface: atom, bridge, and center are considered the possible Na-ion binding sites on undoped GHNS and planar graphene sheets, as shown in Fig. 5b and c. Our calculations reveal that Na-ions preferably bind to the center sites regardless of the shape of the carbon framework; however, the positive binding energies (0.10 eV for GHNS and 0.36 eV for graphene) indicate that the binding of Na ions to GHNS and graphene is thermodynamically unfavorable, as summarized in Table S2. On the other hand, binding of Na-ions to S- and N-doped 3D structures are found to be thermodynamically favorable. Therefore, Na-ions spontaneously tends to bind N- and S-doped structures (Fig. 5d), and the calculated adsorption energies are −2.08 and −0.17 eV for the former and latter sites, respectively. Although, the model structure of the CNT framework has a smaller diameter (~0.8 nm) than the synthesized nanostructures, the calculation results from small model can still provide meaningful insight on the advantage of nitrogen and sulfur doping, since the Na binding ability and the diffusion kinetics calculated from a larger model (diameter of ~1.4 nm) showed similar results (shown in Table S3). This result clearly indicates that N and S doping is an effective strategy to enhance Na-ion binding, which can translate to a higher capacity. Furthermore, Na-ion diffusion in the 3D GHNS structure is very facile, as shown in Fig. 5e–f (activation barrier of ~150 meV), considering that the activation barrier for Na-ion diffusion in typical inorganic Na intercalation hosts is in the range of 300–400 meV. For instance, $Na_{0.66}[Li_{0.22}Ti_{0.78}]O_2$ has an activation barrier of 400 meV and a single layer of graphene like MoS_2 has an activation barrier of 1200 meV [56]. This superior Na-ion diffusion kinetics at the surface of 3D GHNS structures is favorable for achieving faster reaction kinetics. We have also compared the effect of CNT radius on the Na-ion binding ability in which the diffusion kinetics is minimal.

2.2. Cathodic performance

The cathodic (ClO_4^- adsorption/desorption) performance of NS-GHNS has been investigated in the range of 2.5–4.2 V (*vs.* Na/Na^+). From Fig. S11, the CV traces of NS-GHNS clearly exhibit a broad rectangular shape, indicating a typical capacitive behavior attributed to ClO_4^- anion adsorption/desorption. The curves preserve the rectangular shape even at a high scan rate (50 mV s^{-1}), indicating the excellent rate capability of the NS-GHNS cathode. Fig. 6a shows the linear CD curves of NS-GHNS at different current rates, confirming the capacitive-type surface reaction [57]. Further, we have evaluated the rate performances of NS-GHNS and GHNS at different current densities, and the results are compared in Fig. 6b. The NS-GHNS cathode exhibits discharge capacities of ~52 and ~19 mAh g^{-1} at current densities 0.2 A g^{-1} and 20 A g^{-1}, respectively. A porous morphology with a large number of mesopores contributes to the high capacity during the adsorption/desorption process. There could also be some interaction between sodium ions with oxygen functionalities

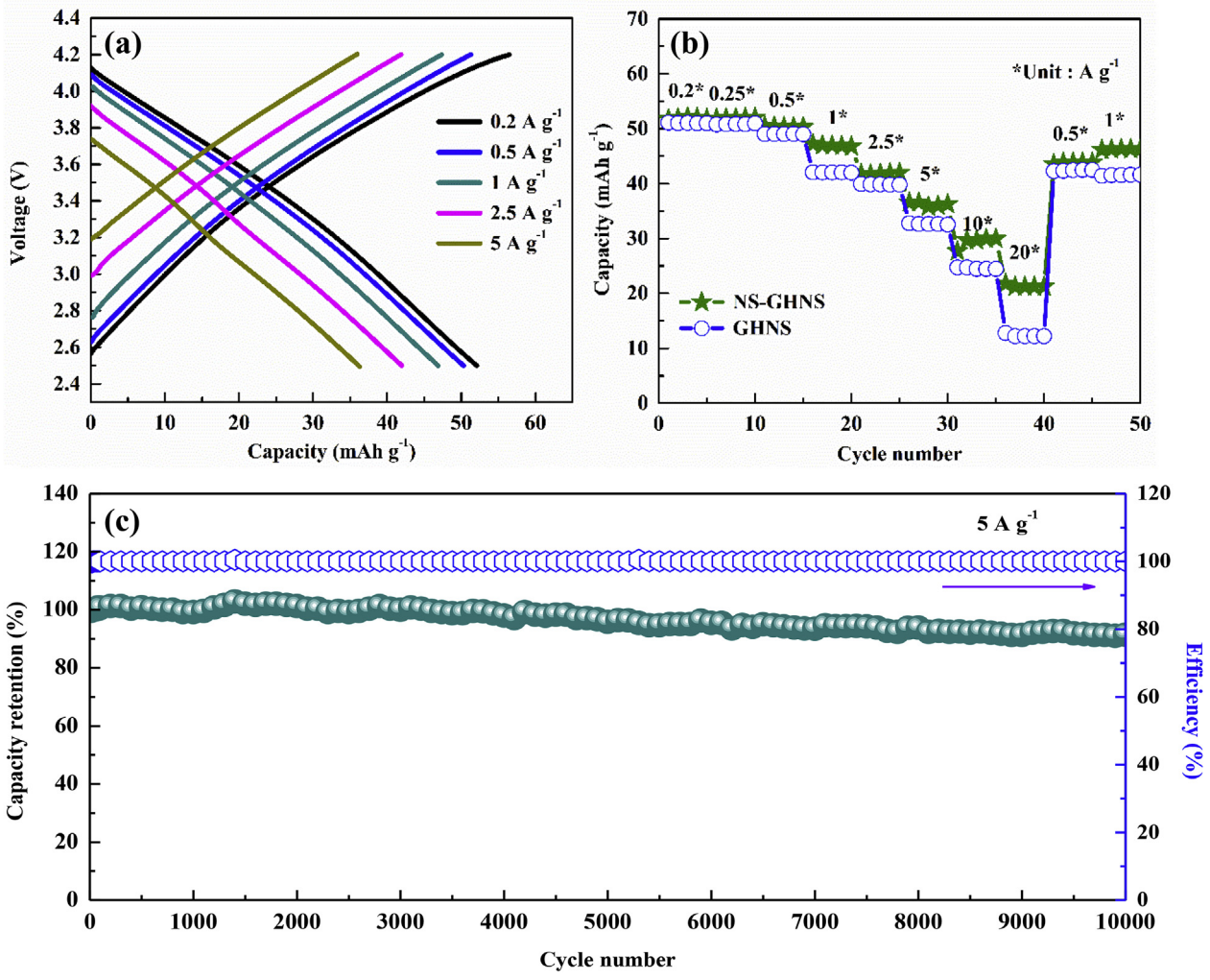

Fig. 6. Cathodic performance of NS-GHNS: (a) Charge/discharge profiles at different current rates, (b) Rate performances of NS-GHNS and GHNS, and (c) Cyclic stability at 2.5 A g^{-1}.

and sulfur hetero atoms through pseudocapacitive reactions. Such interactions would be minimal as hetero atoms available are very low and no obvious peaks from pseudocapacitance contribution are observed from CV and CD curves. Although the discharge capacities of pristine GHNS are similar to NS-GHNS at low current densities (51 mAh g^{-1} at 0.2 A g^{-1} for pristine GHNS), a significant difference is witnessed at higher current densities (12 mAh g^{-1} at 20 A g^{-1} for pristine GHNS). The improved capacitive behavior of the NS-GHNS is mainly attributed to a large number of active surface sites for anion adsorption. In addition, the NS-GHNS cathode exhibits excellent stability with 92% capacity retention even after 10,000 cycles at 5 A g^{-1} (Fig. 6c), demonstrating its high applicability (as a cathode) for NICs perspective. It should be noted here that several capacitor type cathodes for Li/Na-ion capacitors show a notable capacity degradation within a few hundred cycles (<1000) while NS-GHNS showed excellent retention even after 10,000 cycles. This clearly suggests the possibility of using as prospective capacitor type component towards building a highly stable NIC.

2.3. EDLC performance

To further elucidate the capacitive performance of NS-GHNS, EDLCs were constructed with fresh NS-GHNS electrodes in a symmetrical configuration with the same electrolyte ($NaClO_4$ in EC-DEC mixture). The CV curves of EDLCs based on NS-GHNS in Fig. 7a display typical rectangular shapes; the curves do not exhibit any distortion even at 3 V. Notably, at high scan rates, the rectangular profile is very well maintained, without polarization. The CD curves in Fig. 7b are triangular, indicating a perfect double layer formation across the electrolyte-electrode interface [58]. The NS-GHNS-based EDLC exhibits high specific capacitances of 117 and 83 F g^{-1} at 0.5 and 50 A g^{-1}, respectively. On the other hand, the pristine GHNS-based EDLC shows a lower discharge time than the NS-GHNS-based EDLC (Fig. S12a) and specific capacitances of 115 and 37 F g^{-1} at 0.5 and 50 A g^{-1}, respectively (Fig. 7c). Even when the current density increases by a factor of 100, the NS-GHNS-based EDLC retains ~71% of the initial specific capacitance, but the pristine GHNS-based EDLC retains only 32% of the initial capacitance. This superior capacitive behavior of NS-GHNS-based EDLC compared to GHNS-based EDLC is mainly attributed to an enhanced Na-ion accessibility to a large number of pores and improved electron transfer kinetics resulting from the N- and S-doping. This can further be elucidated from the impedance spectra of GHNS- and NS-GHNS-based EDLCs (Fig. S12b), which reveal a smaller charge transfer resistance for the EDLC with NS-GHNS than that with GHNS. In addition, the NS-GHNS-based EDLC exhibits robust stability and impressive capacity retention of ~94% even after 10,000 cycles with >99% coulombic efficiency (Fig. 7d), accounting to an ultra-low capacitance decay of 0.0006% per cycle when tested at 10 A g^{-1}. Notably, high life expectancy in the non-aqueous electrolyte is crucial for achieving a highly stable energy storage system.

2.4. A full nanocarbon based sodium-ion capacitor

The excellent performance of NS-GHNS as both anode and cathode is ascribed to the 3D hollow nanostructure, high surface area with large porosity, and in particular, the presence of rich N and S species on the graphene framework. Considering the aforementioned merits, we

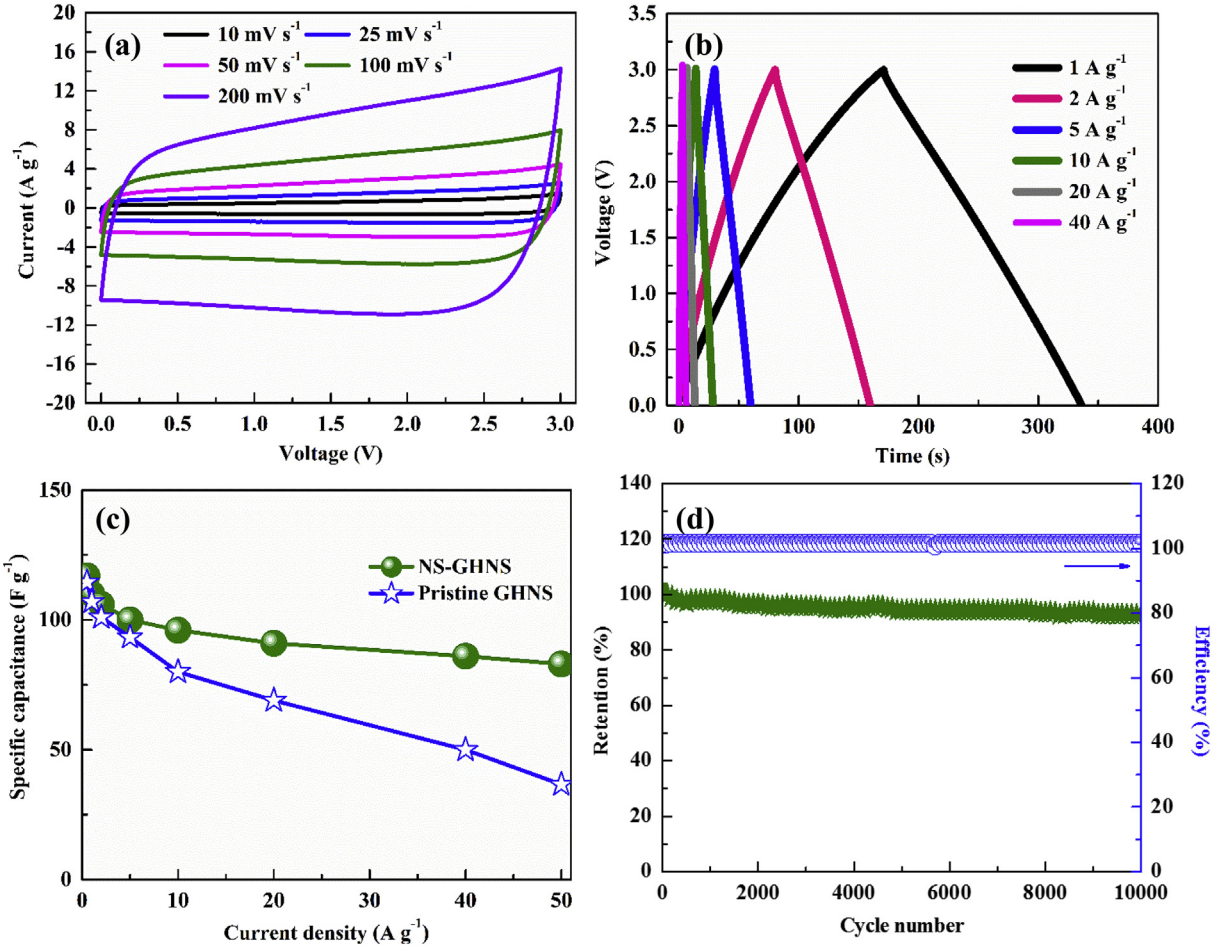

Fig. 7. EDLC performance of NS-GHNS: (a) CV curves, (b) Charge/discharge profiles, (c) Rate performances of NS-GHNS and GHNS, and (d) Cyclic stability at 10 A g^{-1}.

constructed a full nanocarbon based NIC with NS-GHNS as both the anode and the cathode. To achieve a high operating potential for NIC, an NS-GHNS electrode was presodiated; this is an indispensable step to overcome the ion loss in the early cycles upon SEI layer formation [59–61]. In addition, presodiation step allows a large potential difference between the anode and the cathode and significantly enhances the energy density. Fig. 8a illustrates the working process of the presodiated–NS–GHNS//NS-GHNS based NIC. During charge, a large number of Na^+ ions enter NS-GHNS *via* the pseudocapacitive storage, whereas the anion, ClO_4^- adsorb on the pores, edge sites, and the surface of NS-GHNS [59–61]. The process will be reversed during discharge. Fig. 8b shows the typical CV traces of the all carbon based NIC; the curves were obtained at different scan rates in the high voltage range of 1.5–4.2 V. The NIC with NS-GHNS can be charged to 4.2 V, but symmetrical EDLCs can be charged only in a small voltage window of up to 3 V. The high-voltage operation (1.5–4.2 V), in turn, produces a high output energy [59–61]. The fabricated NIC exhibits slightly distorted CV curves, indicating multiple charge storage mechanisms involved during the electrochemical reaction. However, at high scan rates, the curve shape is well retained. The shape retention implies the excellent retention characteristic of the all carbon based NIC. The charge-discharge profiles of the NIC at different current densities are given in Fig. 8c. The obtained results are in correlation with those of the CV studies and parallel the two different charge storage mechanisms in NIC.

On the basis of the galvanostatic discharge time, we have calculated the energy and power densities of the NICs (the mass of both electrode

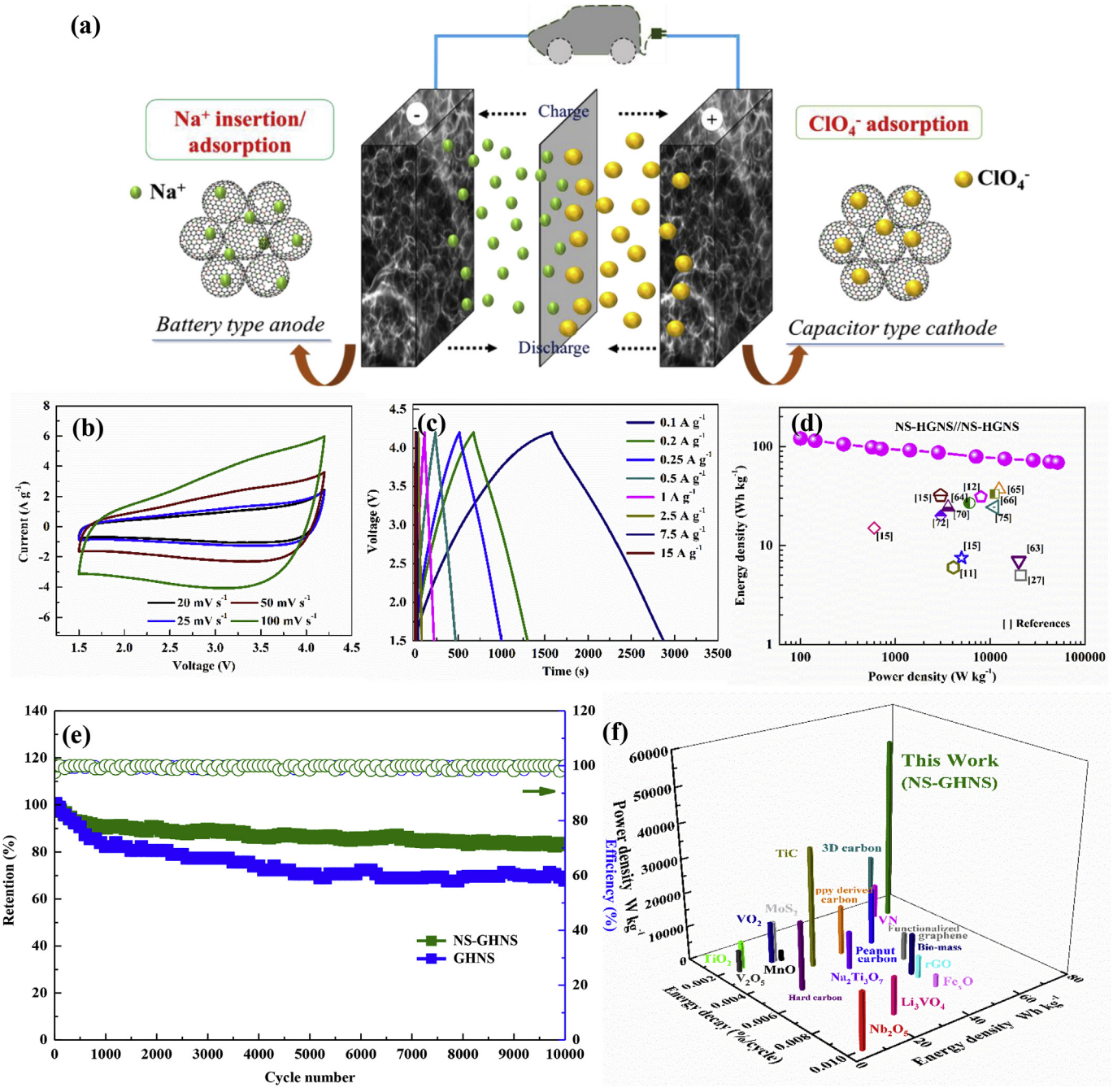

Fig. 8. Electrochemical performance of the NS-GHNS//NS-GHNS NIC: (a) Schematic of working mechanism, (b) CV curves, (c) Charge/discharge profiles, (d) Ragone plot and a comparison with the previously reported results, (e) Cyclic stability at 5 A g^{-1}, and (f) 3D plot comparing the energy-power-cycle behavior of NS-GHNS with that of other devices reported in the literature.

active materials are considered) and compared the data with those from the previous reports. NS-GHNS//NS-GHNS exhibits a high energy density of 121 Wh kg^{-1} at 100 W kg^{-1}, as determined from the Ragone plot in Fig. 8d. At a high power density of 51 kW kg^{-1}, the NIC delivers a remarkable energy density of 69 Wh kg^{-1}, thus demonstrating excellent energy retention at high power densities. The high energy and high power delivery are attributed to the utilization of the same carbonaceous material as both anode and cathode. Furthermore, the Ragone plot compares the maximum power density and energy retention values of the NIC fabricated in this study with those of conventional NICs/LICs. It can be noted from the Ragone plot that the conventional NICs/LICs waste significant energy with increasing power and fails to perform above 20 kW kg^{-1}. The poor behavior severely affects the practical applicability of the energy storage devices, which are required to operate at very high powers. The NIC fabricated in this study significantly retains high energy even at high power rates, and the retention value far exceeds the target for electric vehicle requirements. In addition, the superior performance is similar to the best reported for the state-of-the-art LICs and NICs, such as graphite//activated carbon (AC) (Li^+), graphene-Li_4TiO_{12}//graphene (Li^+), rGO-TiO_2//AC (Li^+), mesoporous-Nb_2O_5//AC (Li^+), graphene-MnO//HNC (Li^+), graphene-Fe_3O_4//3D-graphene (Li^+), Li_3VO_4-nanopeapod//AC (Li^+), graphene-VN//carbon rods (Li^+), Si–SiO_2–C//AC (Li^+), 3D-TiC//pyridine-derived hierarchical porous nitrogen-doped carbon (PHPNC) (Li^+), Nb_2O_5-rGO//AC (Na^+), mesoporous-TiO_2//AC (Na^+), rGO-WO_3//AC (Na^+), rGO-SnO_2//CNT (Na^+), graphene-SnS_2-CNT//Ketjen black (KB) (Na^+), $Na_2Ti_2O_5$//AC (Na^+), $Na_3V_2(PO_4)_3$// biomass carbon (Na^+), rGO-$NaTi_2(PO_4)_3$//graphene nanosheet (GNS) (Na^+), peanut-derived carbon (Na^+), surface functionalized graphene (Na^+), and 3D carbon frameworks (Na^+) [12,40,60,62–75]. Tables S4 and S5 compare the maximum energy density obtained and energy retained at the highest power density for the NIC fabricated in this study with those for several other previously reported LICs and NICs, respectively. Furthermore, we have performed the anode-cathode mass ratio optimization to evaluate the effect of the ratio on the energy power–the behavior of the NIC. The NIC with a ratio of 1:2 performs well, whereas the other ratios of 1:1 and 1:3 exhibit inferior energy–power behavior (Fig. S13). Also, NICs with NS-GHNS display much superior performance compared to the pristine GHNS (Fig. S14). Although both types of NICs delivers similar energies at low power densities, NICs constructed with NS-GHNS retained significantly high energy at high power than GHNS. For instance, the NIC with pristine GHNS delivers only ~35 Wh kg^{-1} at 51 kW kg^{-1}, which is lower than that for the NIC with NS-GHNS. Interestingly, the value obtained for GHNS based assembly is much higher than the other LICs and NICs configurations reported elsewhere. Furthermore, we have evaluated the cyclic stability of NICs with NS-GHNS at a current rate of 5 A g^{-1}. The NICs display excellent charge-discharge reversibility with high energy retention of nearly 85% even after 10,000 cycles as well as maintaining the high coulombic efficiency of >99%. For comparison, we have tested the stability of NICs with pristine GHNS, but the configuration showed the retention of only 70% after 10,000 cycles. Notably, even at a higher operating potential (4.2 V), all NS-GHNS based NIC configuration renders excellent stability owing to the minimal oxygen functionalities compared to the pristine GHNS. In addition, the high energy retention exhibited by NICs with NS-GHNS is attributed to the enhancement in electrolyte-electrode interaction resulting from heteroatom incorporation, which is responsible for a continuous supply of anions and cations (for facile storage). NICs reported in the literature display fast cycle degradation and high energy decay within a few thousand cycles, as can be observed from Tables S4 and S5. The NIC constructed with NS-GHNS displays a low energy loss of ~0.0015% per cycle, which is much lower than that of the state-of-the-art LICs. In addition, the NIC exhibits far superior stability than previously reported LICs/NICs, thereby emerging as a super stable energy storage system. Furthermore, the 3D plot in Fig. 8f compares the energy-power-cycle behaviors of several LICs and NICs; it is clear that the NIC fabricated with NS-GHNS, which displays high energy retention at high power as well as low energy decay, is much superior to the other devices. Thus, the current study highlights the realization of an efficient NIC with identical 3D nanocarbon structures as both anode and cathode; it effectively overcomes the kinetic mismatch, which is observed in the state-of-the-art hybrid capacitors, to achieve remarkable energy, power, and cycle life characteristics.

3. Conclusion

We have successfully developed and demonstrated the high-performance Na-ion capacitor with all N- and S-doped 3D graphene hollow nanospheres as the active material. The NS-GHNS-based configuration displays a remarkable storage capacity, excellent rate performance, and ultra-high durability, outperforming previously reported electrodes for hybrid-ion capacitors. The superior performance of the NS-GHNS based NIC has attributed to a combination of the following merits: a unique 2D material in a 3D hollow nanoarchitecture, numerous N and S heteroatom dopants, high electrical conductivity, high mesoporosity, ultra-fast ion transfer kinetics, and surface-mediated capacitive ion-storage mechanism. In addition, the high-voltage full-nanocarbon Na-ion capacitor with the NS-GHNS bi-functional electrode efficiently overcomes the kinetic mismatch, which is observed between conventional Na^+ battery anodes and capacitor cathodes. Further manipulation of functional groups, size, and morphology can provide a new perspective towards the utilization of nanocarbon materials with 3D architecture for hybrid storage devices to bridge the performance gap between batteries and capacitors.

4. Experimental

4.1. Synthesis of hollow graphene nanospheres

Graphene hollow nanospheres were prepared with amino-functionalized silica templates. In a typical process, first, the silica sphere was synthesized, and then, surface functionalization of was carried out. Silica spheres were synthesized by hydrolyzing tetraethyl orthosilicate (TEOS) in an ethanol/water solution mixture in the presence of ammonium hydroxide catalyst. The hydrolyzed TEOS was allowed to condense for 2 h at ambient conditions with continuous stirring. Then, the solution was filtered, and the precipitate was repeatedly washed with water and ethanol to remove any impurities and subsequently dried in vacuum at 110 °C for 12 h. For surface modification, as prepared silica spheres were dispersed in methanol under the sonication for 30 min and subsequent addition of 3-aminopropyltrimethoxysilane, and the reaction was allowed to proceed for 2 h with continuous stirring at room temperature (25 °C). The as-obtained product was washed several times with methanol and dried under vacuum (110 °C) for 12 h.

To facilitate the preparation of NS-GHNS, we dispersed the amino-functionalized silica spheres in water for 30 min. Subsequently, graphene oxide (GO) was added to the solution in 1:4 GO/amino-functionalized silica weight ratio. The solution was then sonicated for 2 h and stirred overnight to wrap the functionalized silica *via* electrostatic attraction between the positively charged amino functional groups and the negatively charged GO. Subsequently, the solution was centrifuged to remove any free GO and dried at 110 °C for 12 h. In the next step, the sample was thermally treated with thiourea in a tubular furnace at 700 °C for 1 h in under Ar atmosphere to obtain rGO-covered templates. Finally, the template was removed using 10% hydrofluoric acid etching, and the resultant product was washed several times with deionized (DI) water until the pH became ~7. The pristine GHNS were prepared by the same procedure but without the addition of thiourea during the reduction process.

4.2. DFT calculation

First-principles calculations were performed with the Vienna *ab initio*

simulation package (VASP) using projector-augmented wave pseudopotentials implemented in VASP [52–54]. We used Perdew-Burke-Ernzerhof parameterization of generalized gradient approximation to treat the exchange-correlation energies [55]. The activation barrier for Na-ion diffusion at the surface was calculated by the nudged elastic band method [56]. To investigate the effect of CNT radius, we adopted CNTs with two different radii (0.8 and 1.4 nm) as the structural frameworks and separated the structures in the unit cells, under periodic boundary conditions, by more than 10 Å.

4.3. Physical characterizations

Morphologies features of all the prepared samples were examined using a high-resolution transmission electron microscope (HR-TEM, TECNAI, Philips, the Netherlands, 200 keV). An energy dispersive spectrometer attached to the HR-TEM was used to obtain the local elemental distribution [*via* energy dispersive X-ray spectroscopy (EDS)]. Raman spectra of the samples were recorded on a Raman dispersive spectrometer (Lab Ram HR 800, Horiba, Japan). The chemical states of all samples were studied using X-ray photoelectron spectroscopy (XPS) with a Multilab instrument (monochromatic Al Kα radiation $h\nu = 1486.6$ eV). The specific surface area and pore size distribution of the materials were measured by N_2 adsorption/desorption on a Brunauer–Emmett–Teller (BET) analyzer (Micromeritics ASAP 2010) at −196 °C (77 K).

4.4. Electrochemical characterizations

Electrochemical measurements were carried out using standard 2032 coin cells with pure Na-foil as the counter and reference electrodes. For anode fabrication, we first prepared a slurry by thoroughly mixing the active material, carbon black, and sodium carboxymethyl cellulose (CMC) in the weight ratio of 7.5:1:1.5 with DI water. The resultant slurry was coated onto a Cu-foil and then vacuum-dried at 80 °C for overnight. The mass loading for the electrode was about 1.2–1.4 mg cm^{-2}. Similarly, the cathodes were prepared by mixing the active material, carbon black, and the poly (vinylidene fluoride) binder in the weight ratio 7.5:1:1.5 in N-methyl-2-pyrrolidone. The resultant slurry was coated onto a stainless steel foil and then vacuum-dried. The cells were assembled in an Ar-filled glove box with the concentrations of moisture and oxygen below 1 ppm. The 1 M $NaClO_4$ in a mixture of ethylene carbonate (EC) and diethyl carbonate (DEC) (1:1 vol) was used as an electrolyte solution. The electrodes were cycled in the potential ranges of 0.01–3 V and 2.5–4.2 V (*vs.* Na/Na^+) for anode and cathode, respectively. For the fabrication of an all carbon based NIC, the NS-GHNS or GHNS electrodes were galvanostatically cycled for a few cycles against Na metal, which is a general process in the fabrication of NIC to overcome the initial irreversible capacity loss and also ensure the reproducibility of our results. The electrodes were then disassembled and then coupled with another NS-GHNS or GHNS cathode in 2032 coin cells. A symmetrical electric double-layer capacitor (EDLC) was constructed by coupling two fresh NS-GHNS or GHNS electrodes on stainless steel foil in a 2032 coin cell by filling the same electrolyte solution. Cyclic voltammetry (CV) analysis was performed on a Bio-Logic electrochemical workstation (SP-150, France) and galvanostatic charge-discharge measurements were executed with a Won-A-Tech battery tester (WBCS 3000, Korea). The power density (P) was calculated as $P = (I\,V/2)$ (W kg^{-1}), where I is the current density (A g^{-1}) and V is the working voltage (V). The energy density (E) was calculated as $E = (P \times t)$ (Wh kg^{-1}), where t is the discharge time (s).

Acknowledgements

This work was supported by the National Research Foundation of Korea (NRF) grant funded by the Korea government (Ministry of Science, ICT & Future Planning) (No. 2016R1A4A1012224).

Appendix A. Supplementary data

Supplementary data to this article can be found online at https://doi.org/10.1016/j.ensm.2019.09.016.

References

[1] M.S. Whittingham, Chem. Rev. 114 (2014) 11414.
[2] B. Moorthy, S. Kwon, J.-H. Kim, P. Ragupathy, H.M. Lee, D.K. Kim, Nanoscale Horiz. 4 (2019) 214.
[3] Z. Jian, Y.-S. Hu, X. Ji, W. Chen, Adv. Mater. (2017) 1601925.
[4] V. Palomares, M. Casas-Cabanas, E. Castillo-Martinez, M.H. Han, T. Rojo, Energy Environ. Sci. 6 (2013) 2312.
[5] S. Li, J. Chen, X. Gong, J. Wang, P.S. Lee, Small (2018) 1804035.
[6] X. Yu, B. Lu, Z. Xu, Adv. Mater. 26 (2014) 1044.
[7] H. Wang, C. Zhu, D. Chao, Q. Yan, H.J. Fan, Adv. Mater. 29 (2017) 1702093.
[8] S. Chen, J. Wang, L. Fan, R. Ma, E. Zhang, Q. Liu, B. Lu, Adv. Energy Mater. 8 (2018) 1800140.
[9] M.-S. Park, G.K. Veerasubramani, R. Thangavel, Y.-S. Lee, D.-W. Kim, ChemElectroChem 6 (2019) 653.
[10] W. Huanwen, Z. Changrong, C. Dongliang, Y. Qingyu, F.H. Jin, Adv. Mater. 29 (2017) 1702093.
[11] R. Thangavel, A.G. Kannan, R. Ponraj, M.-S. Park, H. Choi, D.-W. Kim, Y.-S. Lee, Adv. Mater. Interfaces 5 (2018) 1800472.
[12] R. Thangavel, B. Moorthy, D.K. Kim, Y.-S. Lee, Adv. Energy Mater. 7 (2017) 1602654.
[13] Z. Jun, L. Wei, Z. Dequn, L. Qinghua, W. Da-Wei, K. Feiyu, Y. Quan-Hong, Adv. Energy Mater. 8 (2018) 1702395.
[14] B. Li, J. Zheng, H. Zhang, L. Jin, D. Yang, H. Lv, C. Shen, A. Shellikeri, Y. Zheng, R. Gong, J.P. Zheng, C. Zhang, Adv. Mater. (2018) 1705670.
[15] J. Ding, W. Hu, E. Paek, D. Mitlin, Chem. Rev. 118 (2018) 6457.
[16] D. Xu, D. Chao, H. Wang, Y. Gong, R. Wang, B. He, X. Hu, H.J. Fan, Adv. Energy Mater. (2018) 1702769.
[17] Z. Jian, V. Raju, Z. Li, Z. Xing, Y.S. Hu, X. Ji, Adv. Funct. Mater. 25 (2015) 5778.
[18] C. Zhu, K. Song, P.A. van Aken, J. Maier, Y. Yu, Nano Lett. 14 (2014) 2175.
[19] T.Y. Zhang, L. Yang, X.B. Yan, X. Ding, Small 14 (2018) 1802444.
[20] S. Ah Ju, K. Kim, J.H. Kim, S.-S. Lee, ACS Appl. Mater. Interfaces 3 (2011) 2904.
[21] Y. Yan, Y.-X. Yin, Y.-G. Guo, L.-J. Wan, Adv. Energy Mater. 4 (2014) 1301584.
[22] J. Xu, M. Wang, N.P. Wickramaratne, M. Jaroniec, S. Dou, L. Dai, Adv. Mater. 27 (2015) 2042.
[23] H. Hou, X. Qiu, W. Wei, Y. Zhang, X. Ji, Adv. Energy Mater. (2017) 1602898.
[24] H. Hou, L. Shao, Y. Zhang, G. Zou, J. Chen, X. Ji, Adv. Sci. 4 (2017) 1600243.
[25] Z.-L. Wang, D. Xu, H.-G. Wang, Z. Wu, X.-B. Zhang, ACS Nano 7 (2013) 2422.
[26] M.S. Kim, E. Lim, S. Kim, C. Jo, J. Chun, J. Lee, Adv. Funct. Mater. 27 (2017) 1603921.
[27] R. Thangavel, A.G. Kannan, R. Ponraj, X. Sun, D.-W. Kim, Y.-S. Lee, J. Mater. Chem. A 6 (2018) 9846.
[28] X. Huang, K. Qian, J. Yang, J. Zhang, L. Li, C. Yu, D. Zhao, Adv. Mater. 24 (2012) 4419.
[29] Y. Huang, Y. Zheng, X. Li, F. Adams, W. Luo, Y. Huang, L. Hu, ACS Energy Lett. 3 (2018) 1604.
[30] G. Zou, H. Hou, G. Zhao, Z. Huang, P. Ge, X. Ji, Green Chem. 19 (2017) 4622.
[31] L. Zhou, Z. Zhuang, H. Zhao, M. Lin, D. Zhao, L. Mai, Adv. Mater. 29 (2017) 1602914.
[32] J. Ding, H. Wang, Z. Li, A. Kohandehghan, K. Cui, Z. Xu, B. Zahiri, X. Tan, E.M. Lotfabad, B.C. Olsen, D. Mitlin, ACS Nano 7 (2013) 11004.
[33] D. Zhang, J. Yang, M. Li, Y. Li, ACS Nano 10 (2016) 10789.
[34] J. Xu, Y. Lin, J.W. Connell, L. Dai, Small 11 (2015) 6179.
[35] S. Dong, Y. Xu, L. Wu, H. Dou, X. Zhang, Energy Storage Mater 11 (2018) 8.
[36] R. Karthick, M. Brindha, M. Selvaraj, S. Ramu, J. Colloid Interface Sci. 406 (2013) 69.
[37] J. Zhang, L. Dai, Angew. Chem. Int. Ed. 55 (2016) 13296.
[38] K. Li, J. Zhang, D. Lin, D.-W. Wang, B. Li, W. Lv, S. Sun, Y.-B. He, F. Kang, Q.-H. Yang, L. Zhou, T.-Y. Zhang, Nat. Commun. 10 (2019) 725.
[39] Q. Lin, J. Zhang, D. Kong, T. Cao, S.-W. Zhang, X. Chen, Y. Tao, W. Lv, F. Kang, Q.-H. Yang, Adv. Energy Mater. 9 (2019) 1803078.
[40] J. Zhang, D.-W. Wang, W. Lv, L. Qin, S. Niu, S. Zhang, T. Cao, F. Kang, Q.-H. Yang, Adv. Energy Mater. 8 (2018) 1801361.
[41] J. Zhang, D.-W. Wang, W. Lv, S. Zhang, Q. Liang, D. Zheng, F. Kang, Q.-H. Yang, Energy Environ. Sci. 10 (2017) 370.
[42] S. Komaba, W. Murata, T. Ishikawa, N. Yabuuchi, T. Ozeki, T. Nakayama, A. Ogata, K. Gotoh, K. Fujiwara, Adv. Funct. Mater. 21 (2011) 3859.
[43] Z. Li, L. Ma, T.W. Surta, C. Bommier, Z. Jian, Z. Xing, W.F. Stickle, M. Dolgos, K. Amine, J. Lu, T. Wu, X. Ji, ACS Energy Lett. 1 (2016) 395.
[44] F. Li, Z. Zhou, Small 14 (2018) 1702961.
[45] D. Li, L. Zhang, H. Chen, J. Wang, L.-X. Ding, S. Wang, P.J. Ashman, H. Wang, J. Mater. Chem. A 4 (2016) 8630.
[46] S. Li, J. Qiu, C. Lai, M. Ling, H. Zhao, S. Zhang, Nano Energy 12 (2015) 224.
[47] L. Zhou, K. Zhang, Z. Hu, Z. Tao, L. Mai, Y.-M. Kang, S.-L. Chou, J. Chen, Adv. Energy Mater. 8 (2018) 1701415.
[48] B. Yang, J. Chen, S. Lei, R. Guo, H. Li, S. Shi, X. Yan, Adv. Energy Mater. (2017) 1702409.
[49] D. Chao, P. Liang, Z. Chen, L. Bai, H. Shen, X. Liu, X. Xia, Y. Zhao, S.V. Savilov, J. Lin, Z.X. Shen, ACS Nano 10 (2016) 10211.

[50] Y. Liu, F. Fan, J. Wang, Y. Liu, H. Chen, K.L. Jungjohann, Y. Xu, Y. Zhu, D. Bigio, T. Zhu, C. Wang, Nano Lett. 14 (2014) 3445.
[51] R. Thangavel, A.G. kannan, R. Ponraj, V. Thangavel, D.-W. Kim, Y.-S. Lee, J. Mater. Chem. A 6 (2018) 17751.
[52] G. Kresse, J. Furthmüller, Comput. Mater. Sci. 6 (1996) 15.
[53] G. Kresse, D. Joubert, Phys. Rev. B 59 (1999) 1758.
[54] P.E. Blöchl, Phys. Rev. B 50 (1994) 17953.
[55] J.P. Perdew, K. Burke, M. Ernzerhof, Phys. Rev. Lett. 77 (1996) 3865.
[56] J. Su, Y. Pei, Z. Yang, X. Wang, RSC Adv. 4 (2014) 43183.
[57] S. Li, J. Chen, M. Cui, G. Cai, J. Wang, P. Cui, X. Gong, P.S. Lee, Small 13 (2017) 1602893.
[58] H. Wang, Y. Zhang, H. Ang, Y. Zhang, H.T. Tan, Y. Zhang, Y. Guo, J.B. Franklin, X.L. Wu, M. Srinivasan, H.J. Fan, Q. Yan, Adv. Funct. Mater. 26 (2016) 3082.
[59] J.H. Won, H.M. Jeong, J.K. Kang, Adv. Energy Mater. 7 (2017) 1601355.
[60] J. Ding, H. Wang, Z. Li, K. Cui, D. Karpuzov, X. Tan, A. Kohandehghan, D. Mitlin, Energy Environ. Sci. 8 (2015) 941.
[61] B. Li, F. Dai, Q. Xiao, L. Yang, J. Shen, C. Zhang, M. Cai, Energy Environ. Sci. 9 (2016) 102.
[62] E. Lim, C. Jo, H. Kim, M.-H. Kim, Y. Mun, J. Chun, Y. Ye, J. Hwang, K.-S. Ha, K.C. Roh, K. Kang, S. Yoon, J. Lee, ACS Nano 9 (2015) 7497.
[63] E. Lim, H. Kim, C. Jo, J. Chun, K. Ku, S. Kim, H.I. Lee, I.-S. Nam, S. Yoon, K. Kang, J. Lee, ACS Nano 8 (2014) 8968.
[64] J. Cui, S. Yao, Z. Lu, J.-Q. Huang, W.G. Chong, F. Ciucci, J.-K. Kim, Adv. Energy Mater. (2017), 1702488.
[65] Y.-E. Zhu, L. Yang, J. Sheng, Y. Chen, H. Gu, J. Wei, Z. Zhou, Adv. Energy Mater. 7 (2017) 1701222.
[66] S. Dong, L. Shen, H. Li, G. Pang, H. Dou, X. Zhang, Adv. Funct. Mater. 26 (2016) 3703.
[67] E. Lim, C. Jo, M.S. Kim, M.-H. Kim, J. Chun, H. Kim, J. Park, K.C. Roh, K. Kang, S. Yoon, J. Lee, Adv. Funct. Mater. 26 (2016) 3711.
[68] R. Wang, J. Lang, P. Zhang, Z. Lin, X. Yan, Adv. Funct. Mater. 25 (2015) 2270.
[69] R. Yi, S. Chen, J. Song, M.L. Gordin, A. Manivannan, D. Wang, Adv. Funct. Mater. 24 (2014) 7433.
[70] L.-F. Que, F.-D. Yu, K.-W. He, Z.-B. Wang, D.-M. Gu, Chem. Mater. 29 (2017) 9133.
[71] Z. Chen, V. Augustyn, X. Jia, Q. Xiao, B. Dunn, Y. Lu, ACS Nano 6 (2012) 4319.
[72] C. Liu, C. Zhang, H. Song, C. Zhang, Y. Liu, X. Nan, G. Cao, Nano Energy 22 (2016) 290.
[73] F. Zhang, T. Zhang, X. Yang, L. Zhang, K. Leng, Y. Huang, Y. Chen, Energy Environ. Sci. 6 (2013) 1623.
[74] Z. Le, F. Liu, P. Nie, X. Li, X. Liu, Z. Bian, G. Chen, H.B. Wu, Y. Lu, ACS Nano 11 (2017) 2952.
[75] S. Chen, L. Shen, H. Lv, P. Kopold, P.A. v Aken, X. Wu, J. Maier, Y. Yu, Adv. Mater. 29 (2017) 1700142.